Published in final edited form as:
Radiother Oncol. 2012 October ; 105(1): 49–56. doi:10.1016/j.radonc.2012.02.011.

Tumour microenvironment heterogeneity affects the perceived spatial concordance between the intratumoural patterns of cell proliferation and ^{18}F-fluorothymidine uptake

Marian Axente[1], **Jun He**[1], **Christopher P. Bass**[1], **Jerry I. Hirsch**[2], **Gobalakrishnan Sundaresan**[2], **Jeffrey Williamson**[1], **Jamal Zweit**[2], and **Andrei Pugachev**[1]

[1]Department of Radiation Oncology, Virginia Commonwealth University Medical Center, 401 College Street, P.O. Box 980058, Richmond, Virginia 23298-0037 (mailing address)

[2]Center for Molecular Imaging, Department of Radiology, Virginia Commonwealth University Medical Center, 1101 E. Marshall Street, 8-022, P.O. Box 980031, Richmond, Virginia 23298-0031

Abstract

Background and purpose—PET imaging with ^{18}F-fluorothymidine (^{18}F-FLT) can potentially be used to identify tumour subvolumes for selective dose escalation in radiation therapy. The purpose of this study is to analyse the co-localization of intratumoural patterns of cell proliferation with ^{18}F-FLT tracer uptake.

Materials and methods—Mice bearing FaDu or SQ20B xenograft tumours were injected with ^{18}F-FLT, and bromodeoxyuridine (proliferation marker). Ex vivo images of the spatial pattern of intratumoural ^{18}F-FLT uptake and that of bromodeoxyuridine DNA incorporation were obtained from thin tumour tissue sections. These images were segmented by thresholding and relative operating characteristic (*ROC*) curves and Dice similarity indices were evaluated.

Results—The thresholds at which maximum overlap occurred between FLT-segmented areas and areas of active cell proliferation were significantly different for the two xenograft tumour models, whereas the median Dice values were not. However, *ROC* analysis indicated that segmented FLT images were more specific at detecting the proliferation pattern in FaDu tumours than in SQ20B tumours.

Conclusion—Highly dispersed patterns of cell proliferation observed in certain tumours can affect the perceived spatial concordance between the spatial pattern of ^{18}F-FLT uptake and that of cell proliferation even when a high-resolution ex vivo autoradiography imaging is used for ^{18}F-FLT imaging.

Keywords

FLT; tumour cell proliferation; mouse tumour; autoradiography; image-guided radiotherapy

Corresponding Author: Andrei Pugachev, PhD, VCU Medical Center, Department of Radiation Oncology, 401 College Street, P.O. Box 980058, Richmond, Virginia 23298-0037; telephone number: (804) 628-3436; fax number: (804) 628-4709; apugachev@mcvh-vcu.edu.

It has been shown that escalation beyond current prescribed doses could increase tumour control in head and neck patients treated with radiotherapy [1]. In order to avoid the normal tissue complications associated with higher doses, treatment adaptation based on PET imaging has been proposed where only tumour subvolumes that are characterized by active cell proliferation and are at high risk for recurrence are receiving escalated doses [2–4]. Histopathological validation is one of the ways to demonstrate that the investigated PET images correctly identify these regions of interest, e.g. characterized by active cell proliferation. Using ex vivo imaging of tumour tissue sections it is possible to obtain images of the intratumoural distribution of PET tracer and compare them to images of specific molecular markers indicative of the targeted biological pathway. Establishing spatial concordance between these two images provides the experimental confirmation that the spatial pattern of the intratumoural PET tracer distribution correctly represents the spatial pattern of the underlying targeted biological features.

3′-deoxy-3′-^{18}F-fluorothymidine (^{18}F-FLT) is currently under consideration as a diagnostic non-invasive imaging marker of tumour cell proliferation, among other tracers (e.g. ^{11}C-methyl thymidine, 1-(2′-Deoxy-2′-^{18}F-1-β-D-arabinofuranosyl)-thymine, 1-(2′-Deoxy-2′-^{18}F-1-β-D-arabinofuranosyl-uracyl)-bromouracil). It was suggested that ^{18}F-FLT PET imaging can be used for image-guided treatment adaptation, since it is a sensitive indicator of early tumour response [3,5]. In vitro validation of this compound has been performed for multiple cancer cell lines, demonstrating its specific uptake in proliferating cells [6]. In vivo studies using both experimental tumour models and patient tumour specimens have demonstrated that ^{18}F-FLT uptake by the tumour as a whole (i.e. maximum or average SUV) correlates well with the labelling index of specific proliferation markers (i.e. Ki-67 labelling index) [7,8]. However, the methodology utilized in these validation studies does not evaluate the spatial co-localization of the pattern of PET tracer uptake with that of biological markers of cell proliferation. Up to date, there are no published data verifying the spatial concordance between intratumoural distribution of ^{18}F-FLT uptake and the pattern of tumour cell proliferation.

Previous histopathological validation studies that sought to demonstrate the co-localization between intratumoural PET tracer uptake and tumour microenvironmental markers used thin tissue autoradiography and microscopy to image the tumour microenvironment. The resulting images were co-registered and pixel-by-pixel intensity correlation analysis was employed to obtain global indicators of spatial co-localization (e.g. Pearson coefficient) between the grayscale intensities in the image-pairs [9–14]. However, this type of analysis is sensitive to many factors that could significantly influence the results. Depending on the ratio of the size of the pixels and the inherent resolution of ^{18}F autoradiography [15–17], local spatial autocorrelation between adjacent autoradiography pixels may occur, invalidating the Pearson correlation assumption of independence between individual pixel values. In addition, the Pearson correlation coefficient is highly sensitive to the presence of noise and non-specific staining/uptake in both considered images (autoradiography and microscopy) [18]. Furthermore, while phosphor plate autoradiography is characterized by linear response over a wide range of signal intensities, the response of the immuno-histochemical microscopic imaging is generally non-linear. Therefore, the Pearson correlation coefficient, which tests the strength of a linear functional relationship between the pixel intensities of two co-registered images, may not be the optimal way to measure the spatial co-localization of these two signals.

Threshold-based approaches provide an alternative and more intuitive approach to analysing the spatial concordance between the pattern of ^{18}F-FLT PET tracer uptake and the pattern of cell proliferation in images from thin tissue specimens. Overlap analysis metrics such as the

Dice coefficient and *ROC* analysis can be used to assess the spatial concordance of the segmented autoradiography and microscopy images.

The goal of this study was to investigate the spatial concordance between the pattern of intratumoural uptake ^{18}F-FLT and the spatial distribution of cell proliferation markers using tumour tissue obtained from small animal xenograft tumour models, and threshold-based image analysis.

Materials and methods

Animal and tumour models

Human head and neck squamous cancer cells were used to establish tumour xenografts in male athymic mice (NCr-nu/nu, National Cancer Institute), from bilateral flank subcutaneous inoculation of 5×10^5 cells/site. Tumour growth was assessed by calliper measurements and recorded every other day. Animal maintenance and all experimental procedures were carried out according to the protocol approved by the local Institutional Animal Care and Use Committee at Virginia Commonwealth University.

Radiotracer synthesis

^{18}F-FLT was produced by the Centre of Molecular Imaging, Virginia Commonwealth University (Richmond, VA). The synthesis followed an established protocol, utilizing 5′-benzoyl-2,3′-anhydrothymidine as a precursor [19,20].

Experimental design

A detailed description of the experimental procedures used in this study was presented before [21]. Briefly, 80 minutes before planned animal sacrifice a bolus injection containing Hoechst 33342 (Sigma-Aldrich, St. Louis, MO) 0.4 mg/20 g mouse, and 37 MBq ^{18}F-FLT was administered by tail-vein injection, followed by two consecutive intraperitoneal injections of bromodeoxyuridine (Sigma-Aldrich, St. Louis, MO) 15 mg/20g mouse, at 50 and at 30 minutes before the animal sacrifice [11]. After sacrifice, the tumours were excised, frozen, and embedded in Tissue-Tek OCT (Sakura Finetek, Japan). From each tumour specimen, several stacks of consecutive 8 μm thick tissue sections were obtained.

Using one tumour tissue section selected from each stack, phosphor plate autoradiography was utilized to image the intratumoural distribution of ^{18}F-FLT [9,22]. The tissue sections were not rinsed previous to the 4 hour exposure at room temperature. ^{14}C standards (American Radiolabeled Chemicals, Inc., St.Louis, Missouri) were simultaneously exposed with the tissue sections. The autoradiography images were digitized at 25 microns per pixel and image intensity values were converted to actual activity (Bq/mm^2).

BrdU uptake was detected on tumour sections after DNA denaturation, by treating the tissue with mouse anti-BrdU monoclonal antibody labelled with Alexa Fluor 594 (Invitrogen) diluted 1:20 in buffer solution. Following immuno-histochemical processing of the tissue sections using the Discovery XT system (Ventana Medical Systems, Inc.), BrdU images of cell proliferation were acquired with fluorescence microscopy (Fig. 1). Routine Mayer's haematoxylin and eosin (H&E) stain was conducted and images were also acquired. All microscopy images were acquired at 20X magnification using a motorized research Olympus BX61 microscope, connected to X-Cite 120PC fluorescence illumination system for immunofluorescence imaging, and an Applied Imaging SL50 automatic microscope slide loader. The automated tiled image acquisition and reconstruction process was controlled through the Ariol software (Genetix, San Jose, CA).

Image processing

The autoradiography and microscopy images were co-registered using a combination of deformable and rigid registration as presented before [21], with an overall registration error of less than 45 μm.

To define the regions of interest, viable tissue masks were obtained from H&E images (Fig 2). First, any non-tumour tissue (muscle, lymphatic tissue) and specimen edges were removed using Photoshop CS4 Extended (Adobe, San Jose, California). These corrected H&E images were processed in MATLAB R2010a (MathWorks), and utilizing colour segmentation and morphological processing, the viable tissue masks were obtained.

To minimize the effect of residual registration misalignments, the autoradiography images were rebinned to 50 μm per pixel, utilizing the mean intensity value for the resulting pixels. A different approach was adopted for the rebinning of proliferation images. In the first step, all non-specific staining that occurred in necrotic parts of the tissue was masked out using the viable tissue mask. In the second step, the corrected images were segmented utilizing a local Otsu thresholding method [23,24]. The resulting mask was used to remove all low-intensity non-specific staining inside the viable tissue, obtaining corrected images of cell proliferation. Since the viable tissue masks were obtained from different (albeit adjacent) tissue sections, manual removal of any remaining high-intensity staining artefacts was performed. In a final step, a global Otsu threshold was applied to the corrected cell proliferation images to obtain only true positive areas of BrdU staining [25]. The resulting binary image was rebinned to 50 μm pixel size, so that the value assigned to each pixel represented the fraction of its area that was positively stained. The resulting image will be referred to as the proliferative cell density image throughout the rest of the study. To preserve consistency in the analysis of the regions of interest, the viable tissue masks were also rebinned to 50 μm per pixel.

Image analysis and statistical evaluation

For the purpose of image analysis, the BrdU-based proliferative cell density images obtained as described above were used to establish the ground truth images of cell proliferation. Specifically, a proliferative cell density was chosen such that the truth set was sensitive enough to include the majority of BrdU positive cells. Therefore, if the 50-by-50 μm unit area contained more than 1% stained surface it was considered a positive. The resulting binary image was defined as the truth set (T).

An instance of the measurement set (M) was obtained by thresholding the FLT autoradiography image. By varying the threshold values from the minimum to the maximum autoradiography intensity levels, a range of measurement sets was obtained. The overlap between the truth set and the measurement sets was analysed as the function of the threshold value. For each FLT threshold value, the following intersection sets were calculated: the true positive set ($TP = T \cap M$), the true negative set ($TN = \bar{T} \cap \bar{M}$), the false positive set ($FP = \bar{T} \cap \bar{M}$), and the false negative set ($FN = \bar{T} \cap \bar{M}$). Using these intersection sets, the Dice coefficient D was calculated [26,27]:

$$D(T, M) = \frac{|T \cap M|}{\frac{1}{2}(|T| + |M|)} = \frac{|TP|}{\frac{1}{2}(|TP| + |FN| + |TP| + |FP|)}$$

Relative Operating Characteristic (ROC) curve analysis [28] was also carried out. This classic test of diagnostic accuracy was adapted to investigate the reciprocal relationship between the sensitivity and specificity of FLT segmentation correctly classifying the pixels

where active cell proliferation occurred. The *ROC* graph depicts on the y-axis the ratio between the number of correctly classified pixels and total number of pixels for each instance of the measurement set, also called sensitivity (or recall):

$$Sensitivity(T, M)=\frac{|TP|}{(|TP|+|FN|)}$$

The x-axis indicates the ratio between incorrectly classified pixels and the total number of pixels, also mentioned as 1-Specificity (or false positive rate):

$$FPR(T, M)=1-\frac{|TN|}{(|FP|+|TN|)}$$

To compare the relative efficacy of this classification method for different scenarios, the area under the curve (*AUC*) was obtained. The *AUC* represents a significant single-value indicator of the expected performance of segmented FLT images correctly representing the spatial distribution of BrdU positive cells.

While ^{18}F autoradiography is characterized by high imaging spatial resolution, it is nevertheless significantly lower than the resolution necessary to resolve microscopic details such as those encountered in the BrdU uptake images. Therefore, partial volume effect results in lowering of the signal and spilling it over into the adjacent regions in the image. To study the influence of image resolution-induced effects on the spatial concordance results, the BrdU images were blurred with a 300 μm Gaussian filter as to create simulated autoradiography images. The size of the blurring kernel was an estimate of the ^{18}F positron autoradiography resolution when imaging with phosphor plates, based on existing literature [15,17,29]. Subsequently, these simulated BrdU autoradiography images were segmented as in the case of the FLT autoradiography, and used to obtain measurement sets in the threshold-based image analysis as described before.

All statistical tests were done utilizing the Statistical Toolbox offered within the MATLAB R2010a (MathWorks) package. Since the data samples were small (8 FaDu tumours, 7 SQ20B tumours), normality of the data could not be clearly demonstrated. Therefore, non-parametric hypothesis testing was utilized, specifically the two-sided rank sum test (Mann-Whitney *U* test). A *P* value less than or equal to 0.05 was considered statistically significant.

Results

Tumour characteristics

Whereas both investigated tumour lines were human squamous head and neck cancers, they expressed different rates and patterns of growth (Fig. 1). FaDu, a human hypopharyngeal cell line produced tumours at least twice as fast as SQ20B (laryngeal origin) for the same calliper-measured volume. Both tumour models present heterogeneous pattern of BrdU DNA incorporation across the tumour section, with higher uptake generally adjacent to well vascularized areas.

ROC analysis

The *ROC* analysis consists of a two-dimensional representation of classifier performance (FLT-positive pixel correctly classifying BrdU positive pixel) and is visualized within the unit square (Fig. 3). Therefore, the *AUC* values were between 0 and 1, with values closer to unity indicating a greater accuracy of the classification method. For FaDu tumours, the

median value for the *AUC* was 0.74 with a range of 0.55–0.84, while for SQ20B tumours the *AUC* median value was 0.51 with a range of 0.42–0.69. The difference in medians was significant at 5% level. Higher values of the *AUC* provide direct evidence of the spatial concordance between the areas of increased activity in the FLT autoradiograms and the areas of increased proliferative cell density.

A sensitivity analysis was also conducted where the variation of the *ROC* curves and *AUC* values was assessed as a function of the threshold value applied to obtain the truth set. Therefore, the measurement sets were compared against more conservative truth sets. These sets were obtained by increasing the minimum proliferative cell density value above which the resulting pixel in the truth set was positive (10% vs. 1%). For FaDu tumours, the new median *AUC* value was 0.73 with a range of 0.5–0.84, not significantly different from the original value. Similarly, for SQ20B tumours, the new median *AUC* value of 0.48 (0.41–0.6), was not significantly different from the value calculated for 1% proliferative cell density. The *AUC* values were still significantly different between the two tumour lines.

Dice coefficient analysis

For each FLT threshold level, a Dice coefficient value was calculated (Fig. 4). The Dice coefficient values indicated the fractional amount of overlap between the segmented FLT area and the BrdU truth set. For FaDu tumours, the median value for the maximum Dice coefficient was 0.61 (range: 0.26–0.77), while for SQ20B it was 0.55 (range: 0.44–0.69). The difference in median values was not statistically significant at 5% level (*P* value = 0.31). A significant difference between the median values of the FLT thresholds at which the maximum Dice coefficient occurred was recorded. For FaDu tumours, it was 38.5%, while for SQ20B tumours it was 7%. As for *ROC* analysis, the sensitivity of overlap analysis as a function of the proliferative cell density threshold value was assessed. Using a more conservative truth set, the maximum overlap decreased, as indicated by a median Dice value of 0.38 for FaDu tumours and 0.16 for SQ20B tumours. The difference in median threshold value at which maximum overlap occurred remained statistically significant between the two tumour lines, 57% for FaDu tumours, and 24% for SQ20B tumours.

Effect of autoradiography resolution

To study how finite imaging resolution-blurring present in autoradiography images affects the results of the analyses presented above, the BrdU microscopy images were convolved with a Gaussian kernel of the same size as the estimated resolution of ^{18}F autoradiography. These blurred BrdU images were used to create the measurement sets, while the high-resolution BrdU images were used to determine the truth set. Whereas there was perfect spatial co-localization between the images used to produce the two sets analysed, the *ROC* analysis indicated less than perfect spatial concordance between blurred BrdU and proliferative cell density images (Fig. 5). FaDu models presented a median *AUC* of 0.92 (0.82–0.95), while for the SQ20B tumours the *AUC* was 0.7 (0.55–0.82). In addition, the overlap analysis indicated that the median value for the maximum Dice coefficient was 0.77 (0.59–0.85) for FaDu tumours and 0.61 (0.49–0.72) for SQ20B tumours.

Discussion

The spatial concordance between intratumoural FLT uptake and the distribution of cell proliferation markers was studied using small animal xenograft tumours representative of human squamous head and neck cancers. The results presented here complement those of previous studies in which ^{18}F-FLT was investigated as a tracer for PET imaging of cell proliferation without addressing the issue of spatial correspondence between the patterns of FLT uptake and cellular proliferation [30–34]. While less important for many diagnostic

applications of FLT PET imaging, the issue of spatial concordance is of utmost importance in radiation oncology treatment planning, where the pattern of uptake of the PET tracer could potentially determine the radiation dose distribution used to treat a patient.

Experimental setup

Some of the experimental details need further discussion. In this study, automated immuno-histopathological processing of the tissue and standardized image acquisition protocols allowed consistent results in obtaining the microscopy images. The necessary confidence in the BrdU-defined truth set definition was further ensured by careful examination and correction of staining artefacts if or when present. In addition, Otsu thresholding has been shown to be one of the most efficient algorithms for segmentation of fluorescent images [23]. As for the sensitivity of the BrdU-defined truth set to the proliferative cell density value used to define the truth set, a preliminary analysis was conducted. *ROC* analysis results were not significantly different, indicating that the specificity of FLT segmentation was consistent in classifying the active proliferation areas indicated by more conservative truth sets. The overlap analysis indicated the expected results for a gradual decrease in extent of the BrdU-defined truth set. This study was based on observations from two tumour lines, utilizing specimens from 15 tumours total. By expanding the study to include more tumours specimens and other cell lines, will allow for further evaluation of FLT images as indicators for determining the spatial distribution of cell proliferation.

FLT for imaging spatial pattern of cell proliferation in FaDu and SQ20B tumours

FLT autoradiography segmentation was the investigated method to retrieve the spatial pattern of cell proliferation. As pointed out by the *ROC* analysis of FaDu tumour data, the median *AUC* value of 0.74 indicated good sensitivity and specificity of the method. In addition, this finding indicates that FLT high-uptake regions in the FaDu tumours are spatially concordant with areas of increased proliferation. Dice coefficient values varied across the range of FLT threshold values selected for particular instances of the measurement sets. The presence of a peak Dice value revealed that there were FLT threshold values for which there was a maximum amount of overlap between the thresholded FLT image and the BrdU-defined truth set. For FaDu tumours, this was achieved at a median threshold value of 38.5%. The fact that the maximum Dice value was not unity (median value: 0.61) is a direct consequence of the truth set being a subset of the investigated region of interest.

For the SQ20B tumours, the maximum amount of overlap between FLT-segmented areas and the truth set was similar, as indicated in the median value of the Dice coefficient (0.55). While not significantly different from FaDu data, these values consistently occurred for very low FLT threshold values (median of 7%). This indicates that for SQ20B tumours, FLT-segmented areas include a maximum amount of the truth set only when the majority of the intensity values were included into the segmented set. Since it is expected that higher intensity values be co-localized with the areas of active proliferation, this result provides direct evidence of the lack of specificity in retrieving the spatial pattern of cell proliferation. *ROC* analysis also supported this finding, where the median *AUC* value was 0.51. The low *AUC* value (representative of random chance in *ROC* analysis) indicates that for this tumour type, the areas of increased FLT uptake were not spatially concordant with the areas of increased proliferation.

Tumour morphology

The results obtained for SQ20B tumour model were unexpected. The experimental methodology was identical for the both head-and-neck tumour models studied. The only fundamental difference between them, that could explain the observed differences, was in

their pattern of growth and the resulting distribution of microenvironmental features. The faster growing FaDu tumours, presented a highly compartmentalized spatial pattern of cell proliferation (Fig. 1). There was uniform BrdU uptake all throughout the well-vascularized area, creating a proliferating rim surrounding hypoxic and necrotic tumour regions. A slow, lobular type of growth induced a dispersed uptake pattern of BrdU in the SQ20B models.

Imaging resolution

Since the microscopic features observed in the cell proliferation images were smaller than the autoradiography resolution, it was necessary to investigate the direct effect of finite imaging resolution on the spatial concordance results. This was done with the aid of the BrdU images blurred with the kernel simulating the resolution limitation of autoradiography images. Thresholding of the blurred BrdU image was less specific at retrieving the spatial pattern of original BrdU staining distribution in SQ20B tumour xenografts, than in the FaDu tumours (Fig. 5). Since the same blurring kernel was applied to both tumour models, this effect could only be caused by the degree of heterogeneity in the spatial distribution of cell proliferation. The SQ20B tumour models had a more dispersed distribution of proliferation markers. Correspondingly, blurring affected these tumours more so than the FaDu tumours, which had a more compartmentalized distribution of cell proliferation. For the latter tumour model, the typical size of the actively proliferating “compartments” was similar or larger than the resolution of autoradiography, therefore blurring did not affect their general spatial distribution. On the other hand, for the SQ20B model, there was no clear compartmentalization of proliferation. After blurring, the typical size of the observed features was significantly larger than of those seen in the original BrdU microscopy image.

FLT-based delineation of actively proliferating tumour subvolumes

When applying the tumour-specific median value for the FLT threshold that produced the maximum overlap between areas of increased proliferation and segmented FLT area, the results were indicative of the difference between the two tumour lines. As emphasized with the blue contour line (Fig. 6), the regions delineated on SQ20B tumours coincided with the whole tissue section area in the majority of cases, while for the FaDu tumours the actively proliferating “compartment” was correctly delineated. To visualize the possibility of misinterpretation of segmented FLT regions, the 50% of maximum intensity threshold value was utilized for images from both tumour lines (red contour, Fig. 6), as a global threshold that is commonly utilized for FLT PET segmentation [35,36]. There were distinct areas delineated in both tumour images. This threshold value resulted in segmented areas that were more conservative, but which were still spatially concordant with areas of increased cell proliferation in FaDu tumours. At the same time, the segmented areas significantly underestimated the extent of the cell proliferation in the SQ20B tumours.

Spatial concordance of FLT uptake and cell proliferation

As illustrated by the xenograft tumour data presented above, tissue morphology and the resulting spatial heterogeneity of cell proliferation, together with imaging resolution, significantly affect the feasibility of using ^{18}F-FLT images to specifically predict the spatial distribution of cell proliferation, as imaged with BrdU. This directly affected the study conclusions about the generality of FLT spatial concordance with cell proliferation. While for FaDu tumours spatial concordance was clearly supported by the data acquired, the same cannot be said about SQ20B tumours. However, this does not imply that there is no spatial concordance between FLT uptake and cell proliferation in the both tumour models at a cellular level. The experiment with the blurred BrdU imaged confirmed that the spatial concordance analysis for SQ20B tumours is inconclusive due to the mentioned combined effect of imaging resolution and spatial proliferation pattern heterogeneity.

In this study, autoradiography images were utilized for delineation of distinct tumour subvolumes of increased cell proliferation. The results indicate the difficulties in this process present even when utilizing autoradiography imaging, which is characterised by the resolution superior to that of any small-animal PET or clinical PET scanners. In PET imaging, the averaging effect induced by positron travel alone can significantly reduce the ability of FLT uptake images to correctly reproduce any map of cell proliferation. It seems that as long as the compartmentalization of the tumour microenvironment presents features that can be resolved with the employed imaging modality, subvolume delineation is feasible. This hypothesis agrees to other studies investigating the ability of ^{18}F-FDG [37] or ^{18}F-FAZA [16] to reproduce the intratumoural distribution of their intended biological target. Further studies of the spatial concordance between the intratumoural pattern of FLT uptake and the spatial distribution of cell proliferation in human pathological samples could elucidate the situations in which imaging with this particular tracer could provide useful information on the spatial distribution of actively proliferating cells.

Conclusion

Within the limitations of the study, we demonstrated that the spatial heterogeneity of the cell proliferation combined with autoradiography resolution significantly affects the feasibility of establishing spatial concordance between the images of FLT uptake and the pattern of the intratumoural cancer cell proliferation. While the spatial concordance between the autoradiography image of FLT and the pattern of cell proliferation was established for FaDu tumours, for the SQ20B tumours, the results were confounded by the finite resolution of autoradiography, which could not resolve the microscopic details of the distribution of cell proliferation.

Acknowledgments

This study was supported by the funds from the Department of Radiation Oncology, VCU and Massey Cancer Centre Support Grant (2P30CA016059-28). The authors would like to acknowledge fruitful discussions and help they received from Ross Mikkelsen, John Wilson, and Mitchell Anscher.

References

1. Lauve A, Morris M, Schmidt Ullrich R, et al. Simultaneous integrated boost intensity-modulated radiotherapy for locally advanced head-and-neck squamous cell carcinomas: II-- clinical results. Int J Radiat Oncol Biol Phys. 2004; 60:374. [PubMed: 15380569]
2. Ling CC, Humm J, Larson S, et al. Towards multidimensional radiotherapy (MD-CRT): biological imaging and biological conformality. Int J Radiat Oncol Biol Phys. 2000; 47:551–560. [PubMed: 10837935]
3. Troost EGC, Bussink J, Hoffmann A, Boerman O, Oyen WJG, Kaanders JHAM. 18F-FLT PET/CT for early response monitoring and dose escalation in oropharyngeal tumors. J Nucl Med. 2010; 51:866. [PubMed: 20484426]
4. Thorwarth D, Geets X, Paiusco M. Physical radiotherapy treatment planning based on functional PET/CT data. Radiother Oncol. 2010; 96:317–324. [PubMed: 20673689]
5. Troost EGC, Schinagl DAX, Bussink J, et al. Innovations in radiotherapy planning of head and neck cancers: role of PET. J Nucl Med. 2010; 51:66. [PubMed: 20009000]
6. Grierson J, Schwartz J, Muzi M, Jordan R, Krohn K. Metabolism of 3′-deoxy-3′-[F-18]fluorothymidine in proliferating A549 cells: validations for positron emission tomography. Nucl Med Biol. 2004; 31:829–837. [PubMed: 15464384]
7. Kenny L, Vigushin D, Al-Nahhas A, et al. Quantification of cellular proliferation in tumor and normal tissues of patients with breast cancer by [18F]fluorothymidine-positron emission tomography imaging: evaluation of analytical methods. Cancer Res. 2005; 65:10104–10112. [PubMed: 16267037]

8. Leyton J, Latigo J, Perumal M, Dhaliwal H, He Q, Aboagye E. Early detection of tumor response to chemotherapy by 3′-deoxy-3′-[18F]fluorothymidine positron emission tomography: the effect of cisplatin on a fibrosarcoma tumor model in vivo. Cancer Res. 2005; 65:4202–4210. [PubMed: 15899811]
9. Carlin S, Pugachev A, Sun X, et al. In vivo characterization of a reporter gene system for imaging hypoxia-induced gene expression. Nucl Med Biol. 2009; 36:821–831. [PubMed: 19720294]
10. Hoeben BAW, Kaanders JHAM, Franssen G, et al. PET of hypoxia with 89Zr-labeled cG250-F(ab′)2 in head and neck tumors. J Nucl Med. 2010; 51:1076–1083. [PubMed: 20554724]
11. Pugachev A, Ruan S, Carlin S, et al. Dependence of FDG uptake on tumor microenvironment. Int J Radiat Oncol Biol Phys. 2005; 62:545–553. [PubMed: 15890599]
12. Busk M, Horsman M, Jakobsen S, Bussink J, van der Kogel A, Overgaard J. Cellular uptake of PET tracers of glucose metabolism and hypoxia and their linkage. Eur J Nucl Med Mol Imaging. 2008; 35:2294–2303. [PubMed: 18682937]
13. Dubois L, Lieuwes N, Janssen MHM, et al. Preclinical evaluation and validation of [18F]HX4, a promising hypoxia marker for PET imaging. Proc Natl Acad Sci U S A. 2011; 108:14620–14625. [PubMed: 21873245]
14. Troost EGC, Laverman P, Philippens MEP, et al. Correlation of [18F]FMISO autoradiography and pimonidazole [corrected] immunohistochemistry in human head and neck carcinoma xenografts. Eur J Nucl Med Mol Imaging. 2008; 35:1803–1811. [PubMed: 18421457]
15. Noguchi J. Imaging plate characteristics of positron emiters: ^{11}C, ^{13}N, ^{15}O, ^{18}F and ^{38}K. Radiochimica Acta. 2001; 89:433–437.
16. Busk M, Horsman M, Overgaard J. Resolution in PET hypoxia imaging: voxel size matters. Acta Oncol. 2008; 47:1201–1210. [PubMed: 18661432]
17. Strome EM, Jivan S, Doudet DJ. Quantitative in vitro phosphor imaging using [3H] and [18F] radioligands: the effects of chronic desipramine treatment on serotonin 5-HT2 receptors. J Neurosci Methods. 2005; 141:143–154. [PubMed: 15585298]
18. Bolte S, Cordelires FP. A guided tour into subcellular colocalization analysis in lightmicroscopy. J Microsc. 2006; 224:213. [PubMed: 17210054]
19. Machulla H, Blocher A, Kuntzsch M, Piert M, Wei R, Grierson JR. Simplified Labeling Approach for Synthesizing 3′-Deoxy-3′-[18F]fluorothymidine ([18F]FLT). J Radioanal Nucl Chem. 2000; 243:843–846.
20. Smyczek-Gargya B, Fersis N, Dittmann H, et al. PET with [18F]fluorothymidine for imaging of primary breast cancer: a pilot study. Eur J Nucl Med Mol Imaging. 2004; 31:720–724. [PubMed: 14991243]
21. Axente M, He J, Bass C, et al. Comprehensive approach to coregistration of autoradiography and microscopy images acquired from a set of sequential tissue sections. J Nucl Med. 2011; 52:1621–1629. [PubMed: 21865287]
22. Pugachev A, Axente M, Humm J. On autoradiographic studies comparing the distributions of ^{18}F- and ^{14}C-labeled compounds in tumor tissue specimens. Radiother Oncol. 2010; 97:609–609. [PubMed: 21074879]
23. Du X, Dua S. Segmentation of fluorescence microscopy cell images using unsupervised mining. Open Med Inform J. 2010; 4:41–49. [PubMed: 21116323]
24. Otsu N. A Threshold Selection Method from Gray-Level Histograms. IEEE Trans Syst Man Cybern. 1979; 9:62–66.
25. Mönnich D, Troost EGC, Kaanders JHAM, Oyen WJG, Alber M, Thorwarth D. Modelling and simulation of [18F]fluoromisonidazole dynamics based on histology-derived microvessel maps. Phys Med Biol. 2011; 56:2045–2057. [PubMed: 21386142]
26. Dice LR. Measures of the Amount of Ecologic Association Between Species. Ecology. 1945; 26:297–302.
27. Shattuck D, Prasad G, Mirza M, Narr K, Toga A. Online resource for validation of brain segmentation methods. Neuroimage. 2009; 45:431–439. [PubMed: 19073267]
28. van Erkel AR, Pattynama PM. Receiver operating characteristic (ROC) analysis: basic principles and applications in radiology. Eur J Radiol. 1998; 27:88. [PubMed: 9639133]

29. Cabello J. The spatial resolution of silicon-based electron detectors in β^+-autoradiography. Phys Med Biol. 2010; 55:1677. [PubMed: 20197603]
30. Salskov A, Tammisetti V, Grierson J, Vesselle H. FLT: measuring tumor cell proliferation in vivo with positron emission tomography and 3′-deoxy-3′-[18F]fluorothymidine. Semin Nucl Med. 2007; 37:429–439. [PubMed: 17920350]
31. Troost EGC, Bussink J, Slootweg P, et al. Histopathologic validation of 3′-deoxy-3′-18F-fluorothymidine PET in squamous cell carcinoma of the oral cavity. J Nucl Med. 2010; 51:713–719. [PubMed: 20395329]
32. Vesselle H, Grierson J, Muzi M, et al. In vivo validation of 3′deoxy-3′-[(18)F]fluorothymidine ([(18)F]FLT) as a proliferation imaging tracer in humans: correlation of [(18)F]FLT uptake by positron emission tomography with Ki-67 immunohistochemistry and flow cytometry in human lung tumors. Clin Cancer Res. 2002; 8:3315–3323. [PubMed: 12429617]
33. Rasey J, Grierson J, Wiens L, Kolb P, Schwartz J. Validation of FLT uptake as a measure of thymidine kinase-1 activity in A549 carcinoma cells. J Nucl Med. 2002; 43:1210–1217. [PubMed: 12215561]
34. Shields AF, Grierson JR, Dohmen BM, et al. Imaging proliferation in vivo with [F-18]FLT and positron emission tomography. Nat Med. 1998; 4:1334–1336. [PubMed: 9809561]
35. Troost EGC, Bussink J, Hoffmann A, Boerman O, Oyen WJG, Kaanders JHAM. 18F-FLT PET/CT for early response monitoring and dose escalation in oropharyngeal tumors. J Nucl Med. 2010; 51:866–874. [PubMed: 20484426]
36. Frings V, de Langen A, Smit E, et al. Repeatability of metabolically active volume measurements with 18F-FDG and 18F-FLT PET in non-small cell lung cancer. J Nucl Med. 2010; 51:1870–1877. [PubMed: 21078791]
37. Christian N, Lee J, Bol A, De Bast M, Jordan B, Grgoire V. The limitation of PET imaging for biological adaptive-IMRT assessed in animal models. Radiother Oncol. 2009; 91:101–106. [PubMed: 19097661]

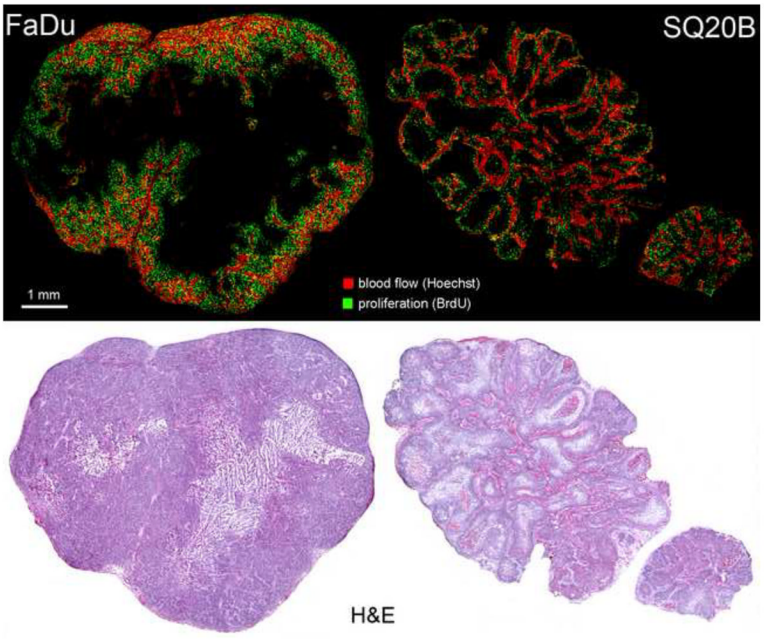

Figure 1.
Representative microscopy images sets for the two tumour models used in this study. Top row shows images of blood flow and cell proliferation. Bottom row shows corresponding H&E image.

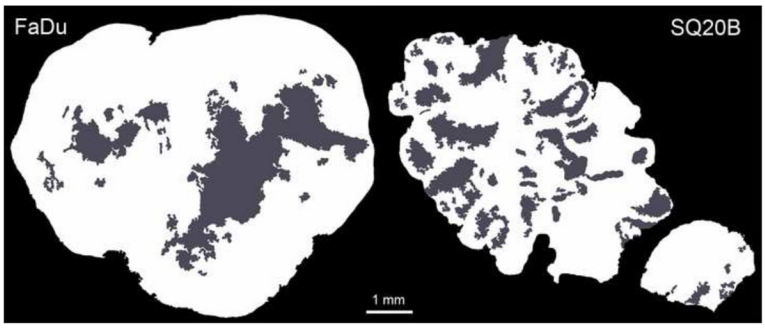

Figure 2.
Viable tissue (shown in white) and necrotic areas (shown in grey) obtained from H&E images. Only the viable tissue is utilized for analysis.

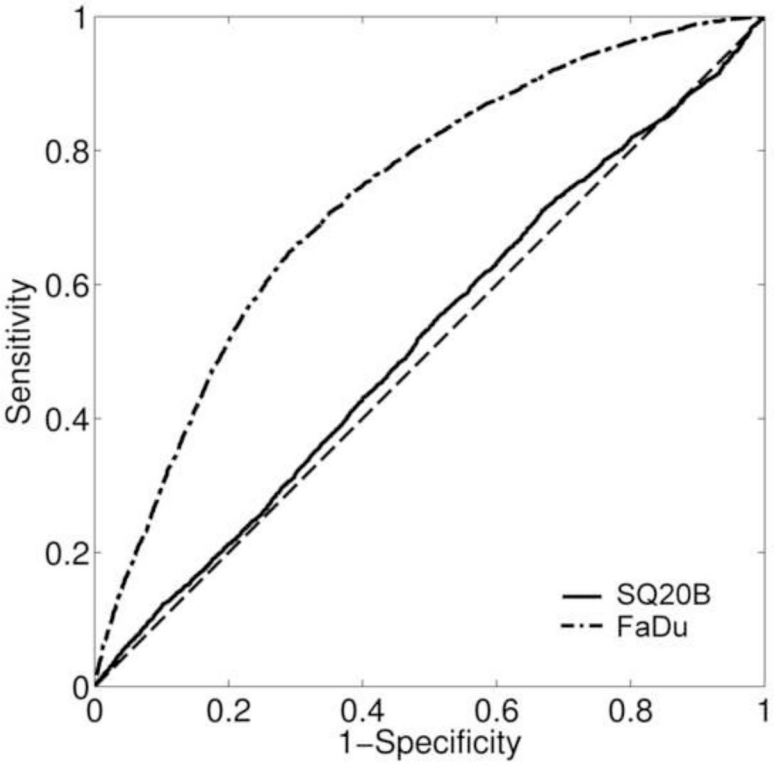

Figure 3.
Examples of ROC curve analysis for utilizing segmented FLT images to predict the spatial distribution of cell proliferation. Presented results were representative of the two tumour specimens presented in figure 2 (AUC_{FaDu} = 0.73; AUC_{SQ20B} = 0.52). The diagonal dashed line (AUC = 0.5) represents the random chance line.

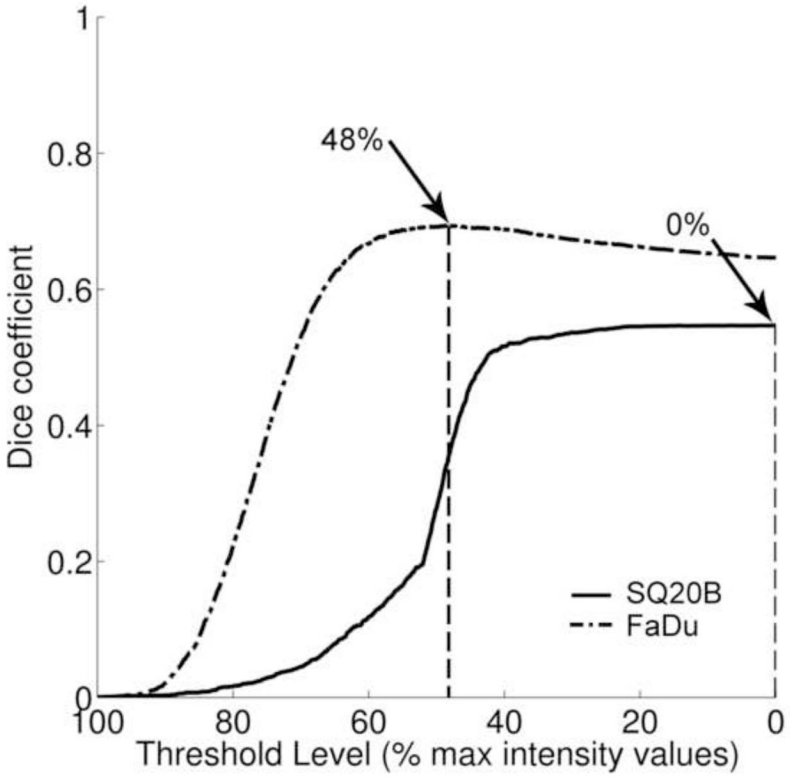

Figure 4.

Dice overlap analysis. Presented results were representative of the two tumour specimens presented in figure 2 ($DICE_{FaDu}$ = 0.69; $DICE_{SQ20B}$ = 0.55). Arrows indicate FLT threshold level for which the maximum Dice coefficient was calculated for the selected tumour sections.

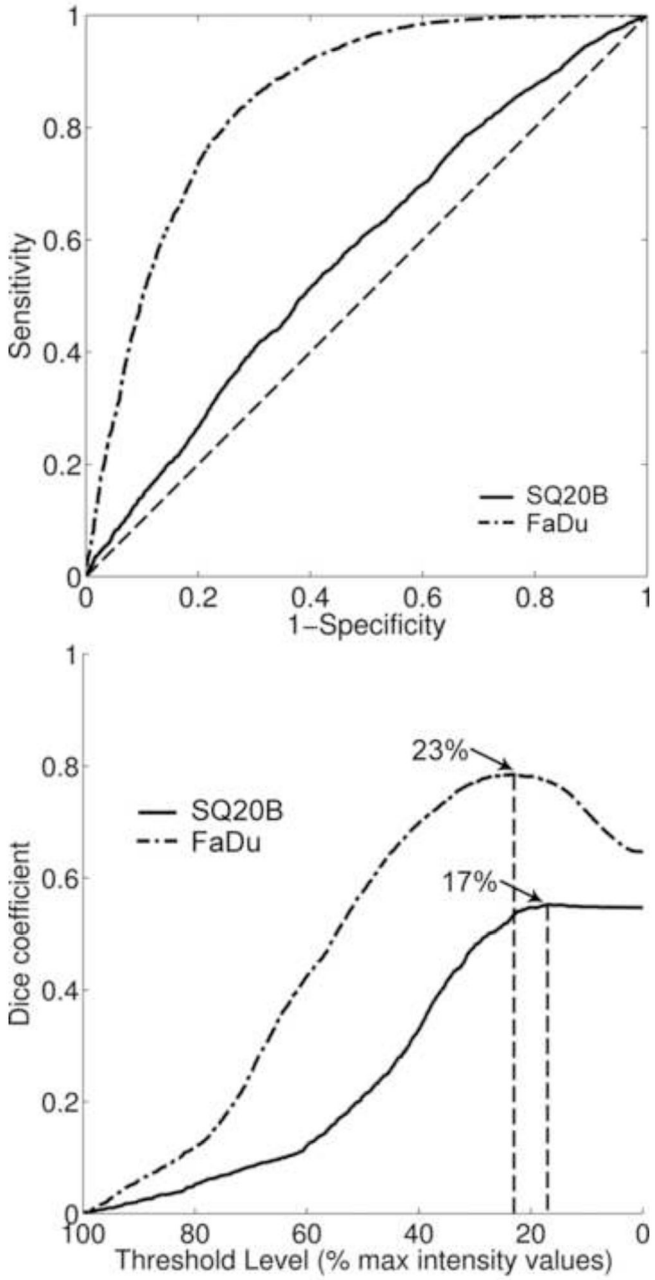

Figure 5.

ROC and Dice analysis of blurred BrdU image vs. BrdU-derived truth set: top panel ROC analysis (AUC_{FaDu} = 0.86, AUC_{SQ20B} = 0.59), bottom panel Dice coefficients vs. threshold levels of blurred BrdU image. Arrows point to the threshold values at which the maximum Dice coefficient occurs ($DICE_{FaDu}$ = 0.79, $DICE_{SQ20B}$ = 0.56).

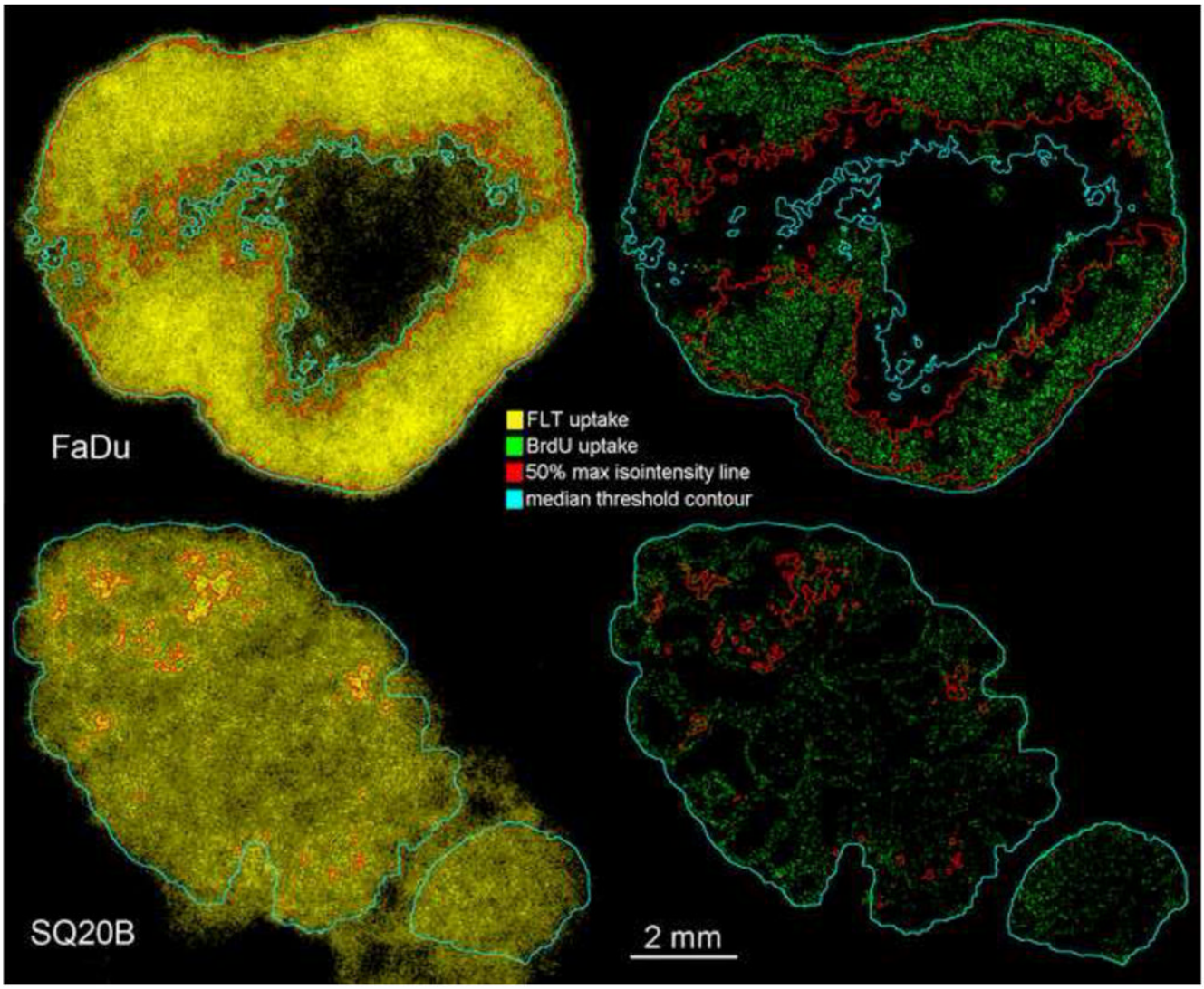

Figure 6.
Tumour subvolumes delineated based on thresholding ^{18}F-FLT autoradiography. FLT threshold contour (iso-intensity) lines were then superimposed on BrdU microscopy images.